nature COMMUNICATIONS

ARTICLE

https://doi.org/10.1038/s41467-020-20521-5 OPEN

Unraveling fundamental active units in carbon nitride for photocatalytic oxidation reactions

Chaofeng Huang[1,2,4], Yaping Wen[3,4], Jin Ma[1,4], Dandan Dong[2], Yanfei Shen[1], Songqin Liu[1], Haibo Ma[3✉] & Yuanjian Zhang[1✉]

Covalently bonded carbon nitride (CN) has stimulated extensive attention as a metal-free semiconductor. However, because of the complexity of polymeric structures, the acquisition of critical roles of each molecular constituent in CN for photocatalysis remains elusive. Herein, we clarify the fundamental active units of CN in photocatalysis by synthesizing CN with more detailed molecular structures. Enabled by microwave synthesis, the as-prepared CN consists of distinguishable melem (M1) and its incomplete condensed form (M2). We disclose rather than the traditional opinion of being involved in the whole photocatalytic processes, M1 and M2 make primary contributions in light absorption and charge separation, respectively. Meanwhile, oxygen molecules are unusually observed to be activated by participating in the photoexcited processes via electronic coupling mainly to M2. As a result, such CN has a higher activity, which was up to 8 times that of traditional bulk CN for photocatalytic oxidation of tetracycline in water.

[1] Jiangsu Engineering Laboratory of Smart Carbon-Rich Materials and Device, Jiangsu Province Hi-Tech Key Laboratory for Bio-Medical Research, School of Chemistry and Chemical Engineering, Medical School, Southeast University, Nanjing 211189, China. [2] Key Laboratory for Green Processing of Chemical Engineering of Xinjiang Bingtuan, School of Chemistry and Chemical Engineering of Shihezi University, Shihezi 832000 Xinjiang, China. [3] School of Chemistry and Chemical Engineering, Nanjing University, Nanjing 210023, China. [4] These authors contributed equally: Chaofeng Huang, Yaping Wen, Jin Ma. ✉email: haibo@nju.edu.cn; Yuanjian.Zhang@seu.edu.cn

Semiconductor photocatalysts have emerged with increasing attention for artificial photosynthesis reactions[1]. Despite enormous advances, developing photocatalysts that have high activity and stability, meanwhile without complex synthetic processes and expensive/toxic elements, is still challenging. Among them, polymeric carbon nitride (CN), consisting of alternatively covalent-bonded C and N atoms, has been stimulated as a prospective candidate with intriguing applications, ranging from solar fuels[2,3], oxidative pollutant remediation[4,5], synthetic organic chemistry to very recent optoelectronic biosensing[6–10], due to its unique electronic structure, exceptional durability under aerobic surroundings and corrosion, and facile preparation using earth-abundant elements[11]. However, owing to slow kinetic processes[12], a substantial enhancement of CN photocatalytic efficiency is highly envisioned.

Along this line, both the extrinsic approaches (e.g., chemical doping[13,14], texture engineering[15–18], and band alignment[19–21]) and the intrinsic routes (e.g., modulation of the condensation degree[22,23], hydrogen content, crystallinity, and surface defects of CN[24–33]) have been pioneeringly explored. For instance, it was disclosed that low molecular weight CN strengthened the reduction ability[22], cyanamide defects enhanced co-catalyst interaction/built-in electric field[23], and N-defects/C–OH terminal groups produced electron trap states[34]. Despite significant advances, the previous studies almost entirely focused on the exploration of a single particular factor/active site influencing the photocatalysis, mainly because of the complexity of polymeric structures. In principle, the acquisition of the critical roles of each featured molecular constituent in CN for the photocatalytic reactions would deepen the understanding of the whole photocatalytic processes and facilitate the precise bottom-up designing and preparing of efficient CN photocatalysts, thus is highly envisioned.

Herein, we clarify the fundamental active units in CN for photocatalytic oxidation reactions through the construction of CN with more defined molecular structures. Enabled by the fast microwave-assisted condensation, the as-prepared CN was verified to mainly consist of melem (M1) and its incompletely condensed form (M2) by a series of careful characterizations. Rather than the traditional opinion of being involved in the whole photocatalytic processes, it was revealed that M1 and M2 were primarily in charge of light absorption and charge separation, respectively; meanwhile, the O_2 substrate was effectively activated by unusually participating in the photoexcited processes via an electronic coupling. As a result, such a configuration of CN endowed it with an exceptional high activity for photocatalytic oxidation of tetracycline (TC) in water.

Results

Preparation of $CN_{MW\text{-}sol}$ and $CN_{MW\text{-}ins}$. A microwave-assisted condensation using ethylene glycol (EG) as the solvent was utilized for synthesizing CN. Compared to the conventional thermal condensation using an electric furnace that generally takes several hours, such fast polymerization in tens of seconds to several minutes which was also reported previously for CN preparation[24,26]. It would promote the synthesis kinetics and maintain the intermediate active sites[35,36], being favor of disclosure of the fundamental active structure-activity relationship of CN. As a result, a higher yield of pale-yellow powder (CN_{MW}) over a yield of 80% was obtained; in contrast, that of traditional bulk CN was only 50–60%. Using ethanol as the solvent, the as-prepared CN_{MW} could be further divided into an insoluble product with a high degree of polymerization ($CN_{MW\text{-}ins}$, yield 70.1%) and a soluble product with a low degree of polymerization ($CN_{MW\text{-}sol}$, yield 12.4%). The general recognized condensation processes are demonstrated in Fig. 1a[23], in which the as-prepared CN consisted of melem (M1) and its incompletely condensed form with cyanide termination (M2).

Structural characterizations of $CN_{MW\text{-}sol}$ and $CN_{MW\text{-}ins}$. In contrast to bulk CN, $CN_{MW\text{-}sol}$ was ready to be disolved, allowing more useful characterization techniques (e.g., the mass spectroscopy) that are rarely used for CN with the aim to disclose more precise molecular structures[37]. According to the general recognized condensation processes[23], M2 was the last intermediate before forming the M1 framework. To support this speculation, the quadrupole-time of flight (Q-TOF) mass spectrometry (MS), which allows samples to be measured directly, was first used to disclose the possible molecular structure of $CN_{MW\text{-}sol}$. As shown in Fig. 1b, the Q-TOF mass spectrum of $CN_{MW\text{-}sol}$ illustrated *m/z* $[M + NH_4^+]$ of 236.1119 assigning to $C_6N_{10}H_6$ (M1, melem, calc.: 218) and *m/z* $[M + H_3O^+]$ of 279.1539 attributable to $C_7N_{12}H_8$ (M2, incompletely condensed form of M1, calc.: 260). The high-performance liquid chromatography-mass spectrometry profile (HPLC-MS, Supplementary Fig. 1) of $CN_{MW\text{-}sol}$ also demonstrated the co-existence of M1 and M2. It should be noted that the intermediates in the early stage of the condensation (theor. molar C/N < 0.56) before the formation of M2 (theor. molar C/N = 0.58) would also be present, but were not likely as the main components in $CN_{MW\text{-}sol}$ (molar C/N = 0.58) and $CN_{MW\text{-}ins}$ (molar C/N = 0.64), considering results from other characterizations such as the combustion elemental analysis (Supplementary Table 1).

The Fourier transform infrared (FT-IR) spectra of $CN_{MW\text{-}sol}$ and $CN_{MW\text{-}ins}$ provided further chemical structures information of M1 and M2 (Fig. 1c). It was observed that both of them exhibited typical vibration peaks around 800 and 1200–1700 cm^{-1}, corresponding to triazine/heptazine rings and CN heterocycles, respectively, similar to that of bulk CN[9]. Nevertheless, notably, the vibration around 800 cm^{-1} for $CN_{MW\text{-}ins}$ exclusively spilt into two comparable peaks, indicating adduct phase of both M1 and M2[38]. Some sharp and broad peaks vibration were also evidently observed for $CN_{MW\text{-}sol}$ and $CN_{MW\text{-}ins}$ ranging from 2900 to 3600 cm^{-1}, which were ascribed to the surface $–NH_x$ group and physically absorbed H_2O molecules[25]. More importantly, a typical vibration for cyanide (C ≡ N) stretch was noted at 2180 cm^{-1} for $CN_{MW\text{-}ins}$[39], and it became more apparent for $CN_{MW\text{-}sol}$, a reliable indicator for incompletely condensed terminal groups in M2. It should be noted that such a cyanamide-terminated group was also observed in CN by conventional thermal condensation[19,23], demonstrating the generality of preparing CN by microwave heating with respect to the traditional electric furnace.

The solid-state NMR was also used to understand the nature of the building blocks of $CN_{MW\text{-}ins}$ with respect to bulk CN networks. As shown in the ^{13}C MAS NMR spectra (Fig. 1d), the presence of heptazine structure in $CN_{MW\text{-}ins}$ can be confirmed by the two resolved resonances for heptazine unit at about 164 (2) and 170 (3) ppm, respectively, which is almost identical to that of bulk CN[30]. Moreover, the ^{13}C signal for the bay carbon of the incompletely condensed M2 was observed at higher chemical shifts (4). Nevertheless, the ^{13}C signal for the carbon atoms in C ≡ N at 112 ppm (see the density functional theory calculation in Supplementary Fig. 2)[19,25,40,41], generally, was weak, manifesting a low content in $CN_{MW\text{-}ins}$, consistent with the result from FT-IR (Fig. 1c) and X-ray photoelectron spectroscopy (XPS, Supplementary Fig. 3) as well[23,30].

The crystalline texture of $CN_{MW\text{-}ins}$ and $CN_{MW\text{-}sol}$ was explored by X-ray diffraction (XRD). As a control, the XRD pattern of bulk CN was also measured, which had two peaks at 13.2° and 27.3°, owing to an in-plane structural packing motif and

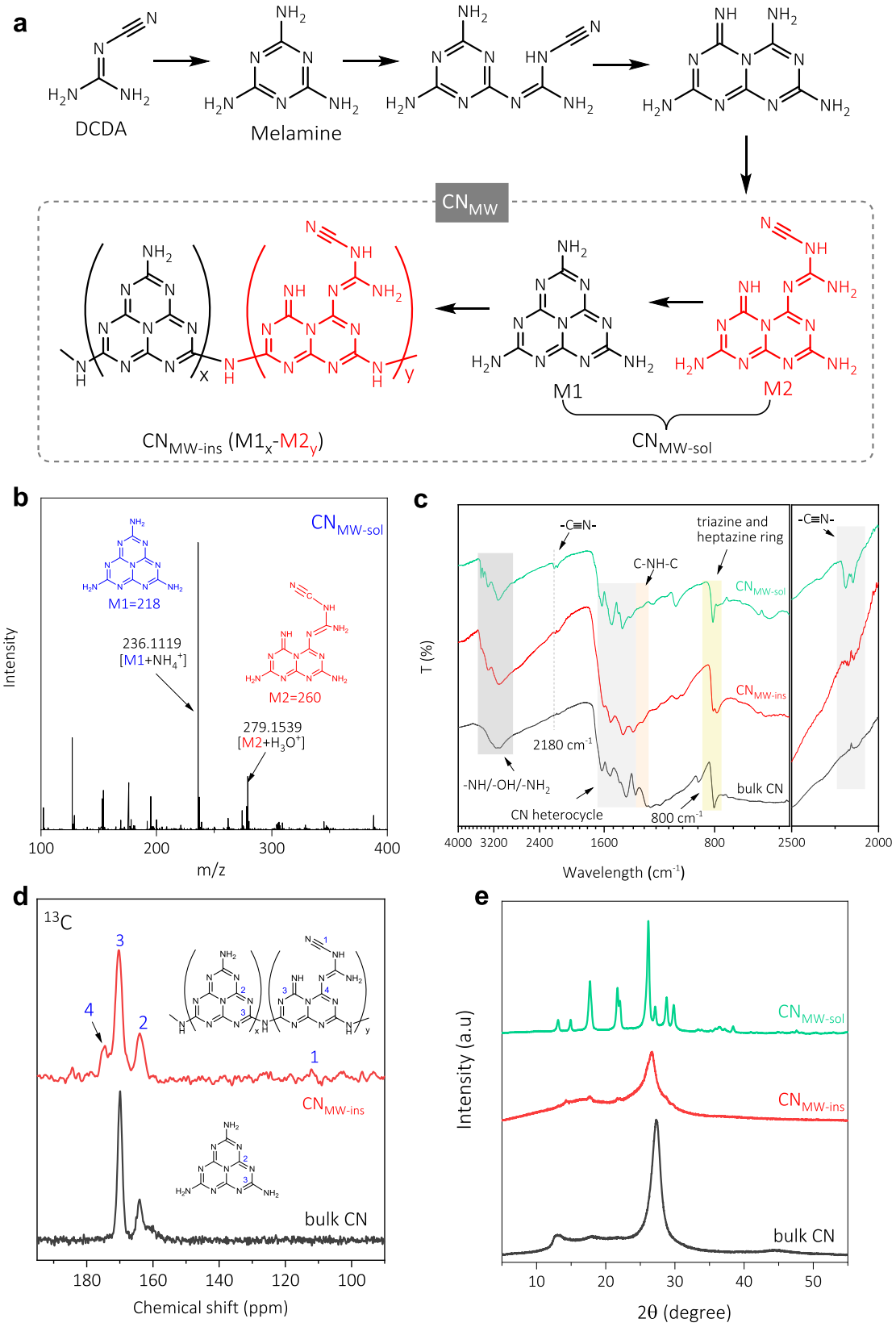

Fig. 1 Structural characterizations of $CN_{MW\text{-}ins}$ and $CN_{MW\text{-}sol}$. **a** Scheme of the general recognized condensation processes for CN_{MW}. **b** Q-TOF mass spectrum of $CN_{MW\text{-}sol}$. **c** FT-IR of $CN_{MW\text{-}ins}$, $CN_{MW\text{-}sol}$, and traditional bulk CN. **d** ^{13}C NMR spectra of $CN_{MW\text{-}ins}$ and bulk CN. **e** Normalized XRD patterns of $CN_{MW\text{-}ins}$, $CN_{MW\text{-}sol}$, and traditional bulk CN.

an interlayer stacking reflection, respectively (Fig. 1e)[15]. Similarly, $CN_{MW\text{-}ins}$ showed a diffraction peak at ca. 26.6°, but down-shift and widened, indicating a slightly enlarged interlayer spacing; meanwhile, the peak located at 13.2° became weak, suggesting weakened crystallinity[15]. In contrast, $CN_{MW\text{-}sol}$ exhibited multiple diffraction peaks, a typical phenomenon for small organic molecules (Supplementary Fig. 4). Consistent with the solubility, it depicted that the condensation degree and the molecular size of $CN_{MW\text{-}sol}$ were smaller than $CN_{MW\text{-}ins}$. In a sense, $CN_{MW\text{-}sol}$ can be regarded as an intermediate of $CN_{MW\text{-}ins}$ during the condensation. To further confirm this assumption, the C/N molar ratio of $CN_{MW\text{-}sol}$ was examined to be 0.58 by combustion elemental analysis (Supplementary Table 1), which was smaller than that of $CN_{MW\text{-}ins}$ (0.64). Moreover, these two ratios located between that of melamine (0.51) and bulk CN (0.68), indicating a moderate depletion of nitrogen during the condensation processes[42].

Therefore, all these structural explorations supported the recognized condensation processes for CN_{MW} (Fig. 1a) with the proposed molecular constituents of M1 and its incompletely condensed form of M2. It would be discussed in the following text that these two primary units, i.e., M1 and M2, played respective roles in light absorption and charge separation/migration in the showcase photocatalytic TC oxidation reaction.

Photocatalytic TC oxidation activity. Apart from widely explored solar fuels generation, the photogenerated electron and hole are valuable in efficient water purification, which is one of the primary considerations for health and safety[43]. For instance, TC is generally recognized as a typical contamination of pharmaceuticals and personal care products (PPCPs) in the environment, and induces the development of antibiotic-resistant pathogens and cause serious problems for human health[44]. Therefore, seeking an economical and environmental-friendly method to remove the PPCPs is essential. Notably, the photocatalytic molecular oxygen activation occurs in a timescale approximately six orders of magnitude faster than molecular oxygen evolution, acknowledged in both natural and artificial photocatalysts[25,27–30]. In this context, the attempt to remove PPCPs by CN photocatalyst with the participation of molecular oxygen was intriguing.

The photocatalytic oxidation of TC by different CN was investigated. As shown in Fig. 2a, the absorbance of TC was reduced by 10% in the presence of $CN_{MW\text{-}ins}$ under the absorption–desorption equilibrium in the dark, which was larger than that by bulk CN, due to the stronger electrostatic interaction between of TC and $CN_{MW\text{-}ins}$ (zeta potential of 37 mV, Supplementary Fig. 5). Moreover, under identical conditions, the $CN_{MW\text{-}ins}$ had a more notable photocatalytic oxidation ability than bulk CN. For instance, after irradiation for 20 min, only ca. 25% of TC was unreacted by $CN_{MW\text{-}ins}$, while that was ca. 70% by bulk CN. As a control, the TC concentration remained almost unchanged without any photocatalysts, which demonstrated that TC was stable under irradiation, and the oxidation activity was exclusively derived from the photocatalysts. For a quantitative comparison of kinetics, the pseudo-second-order rate constant (k) was calculated. Figure 2b showed the k for $CN_{MW\text{-}ins}$ ($1.2502\ mol^{-1}\ m^3\ min^{-1}$) was ca. 6 times of that for bulk CN ($0.2034\ mol^{-1}\ m^3\ min^{-1}$). $CN_{MW\text{-}sol}$ also demonstrated an apparent photocatalytic activity ($k = 1.0986\ mol^{-1}\ m^3\ min^{-1}$), which was further boosted after cooperation with $CN_{MW\text{-}ins}$ as CN_{MW} ($k = 1.5723\ mol^{-1}\ m^3\ min^{-1}$, Supplementary Fig. 6). The even higher activity of the CN_{MW} sample may be explained by the isotype heterojunction of matched electronic band structures between $CN_{MW\text{-}ins}$ and $CN_{MW\text{-}sol}$ that promoted the charge separation (Supplementary Fig. 7)[45–47], rather than the varieties in the geometric structures (see SEM/TEM images in Supplementary Fig. 8). In contrast, only a marginal photocatalytic activity was observed for melamine, M1, and bulk CN, demonstrating the importance of coupling M1 and M2 in synergistically boosting the photocatalytic activity.

The bactericidal halo test was further conducted on Luria–Bertani agar to investigate the antibacterial activity of the oxidized TC by CN_{MW}. As depicted in Fig. 2b inset, the treated TC solution exerted no inhibitory effect on Staphylococcus aureus, as evidenced by the almost invisible inhibition zones. It indicated that the photocatalytic oxidation by CN_{MW} would effectively covert TC into environmental and bio-safe molecules. Besides, CN_{MW} maintained a good photocatalytic performance during three reaction cycles, indicative of reasonable stability (Supplementary Fig. 9). It should be noted that the similar activity trends among different CN samples such as CN_{MW} and bulk CN were also observed for the photocatalytic oxidation of other substrates, such as Azure B (Supplementary Fig. 10)[9].

Mechanism study of CN_{MW} in photocatalytic oxidation. To understand the photocatalytic mechanism, the trapping experiments were carried out to explore the possible intermediate reactive species. It was observed that by adding superoxide, hole, ·OH, or O_2 scavengers, the oxidation efficiency of $CN_{MW\text{-}ins}$ demonstrated a various degree of inhibition (Fig. 2c)[48]. Remarkedly, among them, the oxidation activity was drastically restrained when N_2 was purged into the reaction solution, revealing that O_2 was an important co-substrate and the activation of O_2 by reduction via photogenerated electrons into $O_2{\cdot}^-$ and H_2O_2 (Supplementary Fig. 11) was the major step in the oxidation of TC (Fig. 2d)[49,50].

The UV–Vis spectra (Supplementary Fig. 7a) and photoluminescent spectra (Supplementary Fig. 12) of $CN_{MW\text{-}ins}$ and $CN_{MW\text{-}sol}$ were also measured. It was observed that $CN_{MW\text{-}ins}$ had more light absorption than $CN_{MW\text{-}sol}$. Considering $CN_{MW\text{-}ins}$ had a higher ratio of M1 than $CN_{MW\text{-}sol}$, it suggested that M1 had a more substantial light harvesting with respect to M2. Moreover, it was noted that even $CN_{MW\text{-}ins}$ also demonstrated a much less light absorption than bulk CN, verifying the better activity of $CN_{MW\text{-}ins}$ with respect to bulk CN was not ascribed to the absorption of more photons. As $CN_{MW\text{-}ins}$ contained more M2 than bulk CN, it indicated that M2 may play an essential role in accelerating the charge separation. In this sense, the hole- and electron-extraction properties were evaluated by measuring anodic and cathodic photocurrents, respectively, in the presence of an electron donor (triethanolamine, TEOA), assuming the maximum photocurrent can be obtained without any hole- or electron-transfer limitations[51,52]. As shown in Supplementary Fig. 13, both anodic and cathodic photocurrents at $CN_{MW\text{-}ins}$ were less improved with respect to bulk CN by adding TEOA, indicating superior hole- and electron-extraction properties contributed by M2 during the reaction in aqueous solution.

For more comprehensive mechanism insights of the increased photocatalytic activity, particularly with the critical role of M1/M2 and the participation of oxygen substrates, quantum chemical calculations of monomers, such as M1/M2, M1–M1, M2–M2, and the M1–M2 bonding patterns, were performed (Supplementary Fig. 14). Due to the intrinsic higher conjugation, the simulated absorption spectra showed that M1 had a higher intensity than M2, no matter with (Fig. 3a) or without (Supplementary Fig. 15) interaction with O_2 substrate. It became more evident when two M1 forms a covalent-bonded dimer; after coupling to M2, a suppressed intensity of absorption was observed for M1–M2, but still stronger than M2 monomer or dimer. Consistently,

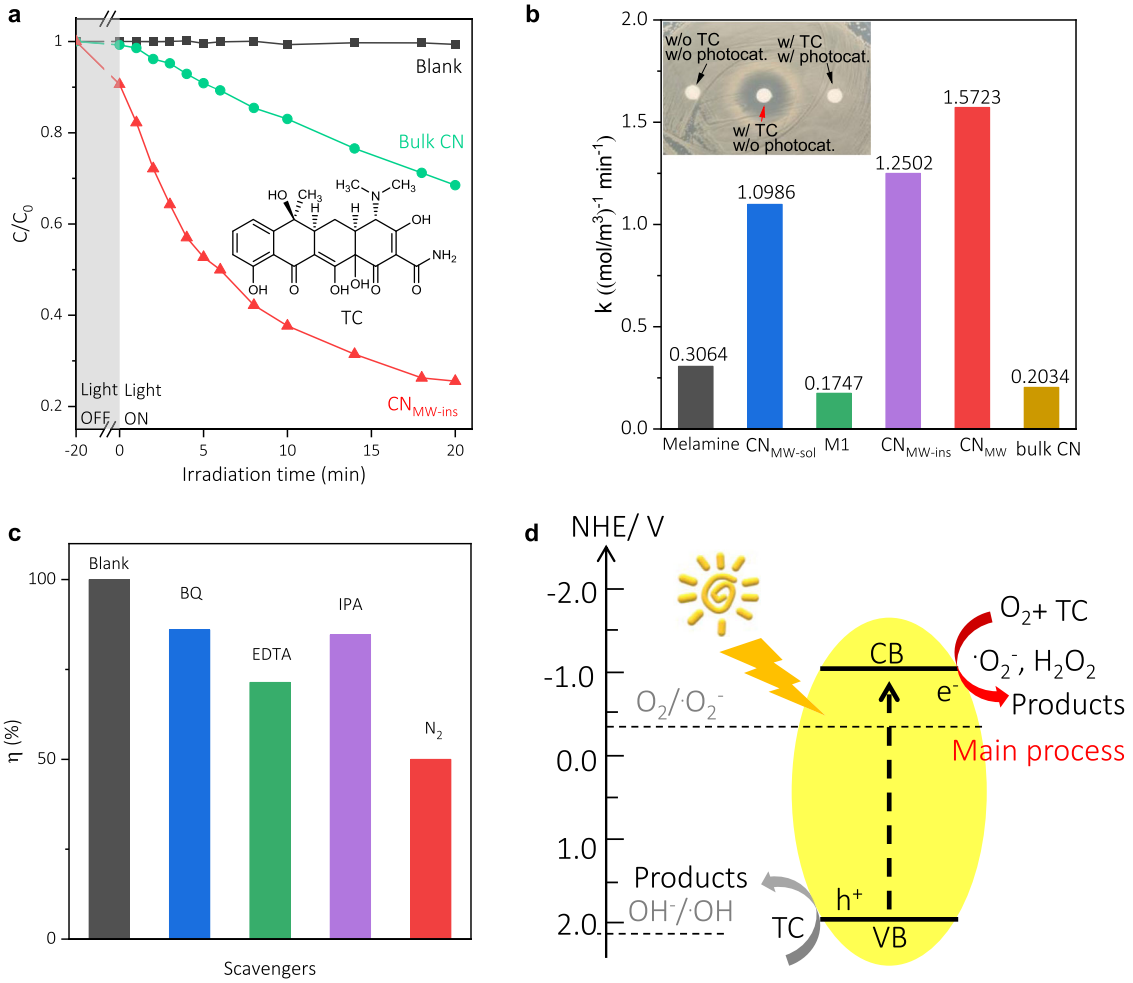

Fig. 2 Photocatalytic sanitation of TC-contaminated water by CN. a Absorbance of TC at 357 nm as a function of time during photocatalytic oxidation reaction (>400 nm) using bulk CN and CN_{MW-ins} catalyst. **b** Pseudo-second-order reaction kinetics for TC sanitation using different photocatalysts. Inset: bactericidal halo test. "w/" and "w/o" denote "with" and "without," respectively. **c** Photocatalytic activity of CN_{MW-ins} for TC sanitation in the presence of different scavengers. **d** Proposed mechanism of photocatalytic oxidation of TC.

presumably owing to a higher ratio of M1, more light absorption of CN_{MW-ins} compared to that of CN_{MW-sol} was also observed in experiments (Supplementary Fig. 7a). These facts exclusively demonstrated the primary role of M1 in light harvesting. Besides, it was also noted that owing to the extension of conjugation, the M1–M2 dimer had an extended absorption edge in longer wavelength with respect to M1 monomer or dimer, indicative of an easier excitation.

In addition to light harvesting, the charge separation/migration was also essential. For this, the spatial distribution of electron and hole populations of M1, M2, and their dimers in the lowest singlet electronic excited state (S_1) without and with the participation of O_2 were simulated (Supplementary Fig. 16) and quantified (Supplementary Table 2). Interestingly, a strong electronic coupling interaction by O_2 substrate was observed. For instance, the electrons and holes of M1 alone were distributed on the whole framework with a large degree of overlapping, while with the participation of O_2 the overlap was noticeably suppressed, making the separation became more effective (see the quantitative centroids distance in Fig. 3b). Note that the substrates-associated electronic coupling to the light absorption and charge separation/migration was essential, especially in photocatalytic oxidation reactions, but has been rarely studied and poorly understood. Moreover, due to the strong electron deficiency of cyano group in M2, the electron–hole separation became evident in M2 and more significant in M1–M2.

The electron distribution of the frontier molecular orbitals of all O_2@CN in S_1 was further depicted in Fig. 3c. It was observed that the excitation energy of S_1 (E_{S1}) in M1–M2 was the lowest, indicating the easiest excitation. Notably, for the highest occupied molecular orbital, the electrons were only localized on the CN molecules. In contrast, for the lowest unoccupied molecular orbital (LUMO), the electrons in the O_2@M1 and O_2@M2 were mainly contributed by O_2, and that in O_2@M1–M1 and O_2@M2–M2 systems were primarily distributed in CN framework.

Interestingly, the electrons in O_2@M1–M2 were distributed in both O_2 and CN framework (primarily of M2). Moreover, the quantified contribution of O_2 in M1–M2 (4.74%) was greater than that in O_2@M1–M1 (−0.06%). Thus, compared to M1–M1, M1–M2 was more likely to be excited along with a higher contribution of O_2 in LUMO, i.e., more conducive to activate O_2 in the following oxidation reaction. Such trends could also be observed by the uneven distribution of the electron density of the whole structure with M1 and M2 (Supplementary Fig. 17). Notably, the more detailed structures and properties of the CN photocatalysts and the oxidation products would be very interesting and deserve a future investigation. Briefly, the photoexciting processes for O_2@M1–M2 were summarized in

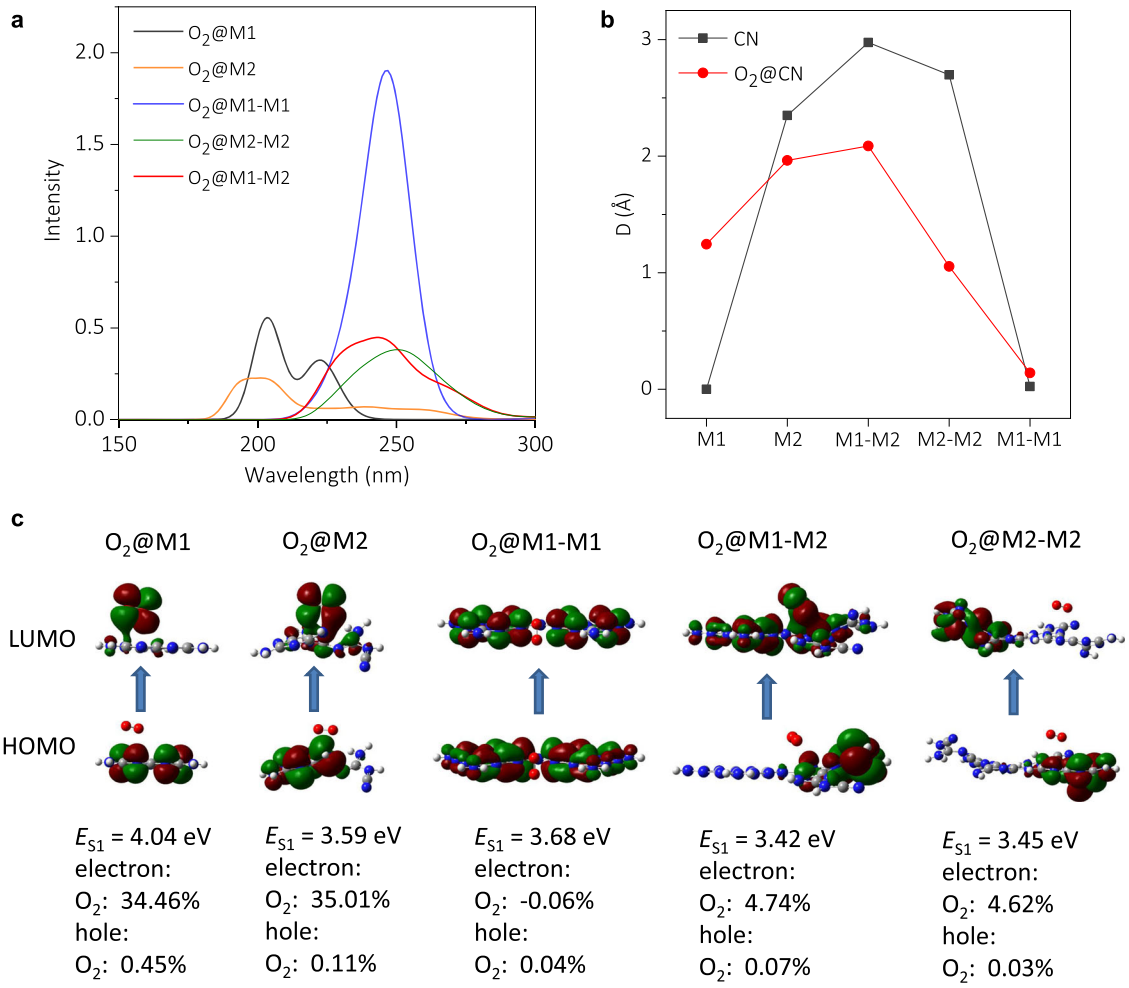

Fig. 3 Computational analysis of M1, M2, and electron coupling. a Simulated absorption spectra of O_2@CN. **b** Centroids distance (*D*) of electrons and holes in the lowest singlet electronic excited state (S_1) of CN and O_2@CN. **c** Isosurface plots of the highest occupied molecular orbital (HOMO) and the lowest unoccupied molecular orbital (LUMO) of different O_2@CN. The excitation energy (E_{S1}) and the percentage of O_2 contribution to electrons and holes in S_1 are shown in the bottom panel.

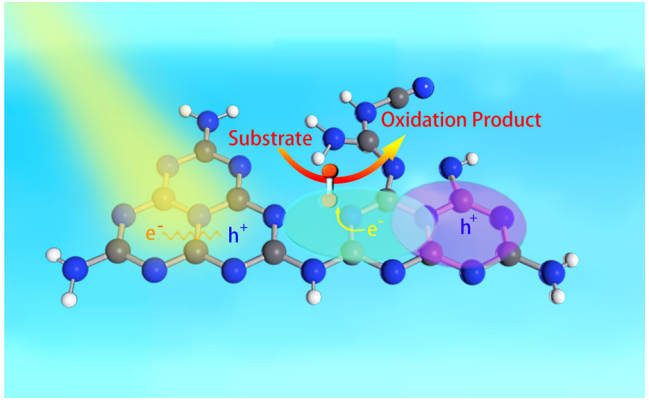

Fig. 4 Roles of each molecular constituent in carbon nitrides. Scheme of the light harvesting and the spatial distribution of electron/hole on M1-M2 framework with the electron coupling of O_2.

Fig. 4. It is highly envisioned that the acquisition of the critical roles of each featured molecular constituent in CN for the photocatalytic reactions would reshape the understanding of the whole photocatalytic processes and facilitate the precise bottom-up designing and preparing of efficient CN photocatalysts.

Discussion

In summary, we report the preparation of CN_{MW} consisted of molecular constituents of melem (M1) and its incomplete condensed form with cyanide termination (M2) by a microwave-accelerated condensation in tens of seconds. Both experiments and theoretical analysis revealed that M1 and M2 intriguingly made a predominated contribution in light absorption and charge separation, respectively. Meanwhile, the oxygen substrate was surprisingly observed to participate in the photoexcited processes via an electronic coupling process, mainly to M2 in the final CN_{MW}. As a result, an exceptional boosted photocatalytic activity for TC oxidation by CN_{MW} was observed up to eight times over the conventional bulk CN. The more detailed understanding of the critical roles of each fundamental active unit and their synergistic effects would substantially pave the way for rational bottom-up preparation and practical applications of CN and other emerging polymeric photocatalysts as well in energy, environmental remediation, and beyond, such as prospective optoelectronic biosensing.

Methods

Reagent. The following chemicals were obtained as indicated: dicyandiamide (DCDA, 99%, Sigma-Aldrich), TC (98%, Aladdin), isopropanol (IPA, 99.8%, Aladdin), ethylenediaminetetraacetic acid disodium salt (EDTA, 99%, Sinopharm chemical Reagent), benzoquinone (BQ, 99%, J&K), and EG (99%, Sinopharm chemical Reagent). All chemicals were used without further purification, unless

otherwise specified. Ultrapure water (18.2 MΩ cm) was obtained from a Smart2 water purification system (Thermo Scientific, USA).

Preparation of bulk CN and M1. Bulk CN was prepared by heating DCDA for 4 h to 550 °C and kept at this temperature for 4 h in air. The final product was ground into fine powder and used without further purification. The M1 sample was prepared, according to the previous study of polymerization kinetics of bulk CN. Briefly, it was synthesized by condensation of DCDA at 390 °C in a muffle furnace.

Microwave-assisted synthesis of CN_{MW}. First, 20 g of DCDA precursor was added into 200 mL of EG (owning a high loss factor tan δ of 1.350, due to efficient electromagnetic radiation absorption and rapid heating, boiling point: 198 °C) under stirring at 70 °C for 15 min, at the end of which, the Tyndall effect was normally not observed, indicating the formation of a true solution instead of a colloidal system. Second, 5 mL of DCDA/EG solution was added into a crucible and placed into a microwave reactor (700 W, M1-L213B, 2.45 GHz, Midea, China), and then irradiated for several 10 s (typically of 90 s). The resulting sample was denoted as CN_{MW}. Then, CN_{MW} was stirred in ethyl alcohol for several hours to separate the insoluble part denoted as $CN_{MW\text{-}ins}$ and soluble part denoted as $CN_{MW\text{-}sol}$.

Photocatalytic oxidation of tetracycline. Briefly, 100 mg of photocatalyst was added in a quartz tube (5 × 5 × 5 cm, 20 mL) of 0.05 mg/mL TC aqueous solution. First, the suspension was stirred for 20 min in dark to ensure the establishment of adsorption equilibrium. Afterwards, the quartz tube was top-irradiated under full light by using a 300 W Xe lamp (CEL-HXUV300E, China) with a short-pass filter cutting off lights of wavelength less than 400 nm. 0.4 mL of suspension was extracted and centrifuged at certain time intervals. The photocatalytic oxidation efficiency of TC at 357 nm was analyzed on the UV–Vis spectrophotometer. In order to investigate the main oxidation species of the photocatalytic reaction, IPA, EDTA disodium salt, and BQ were selected as the scavengers for ·OH, h^+, and $\cdot O^{2-}$, respectively. The concentration of these scavengers was 0.1 mM.

Characterization. The FT-IR spectra were recorded with a Nicolet 4700 (Thermo, USA) equipped with an attenuated total reflection setup. The UV–Vis absorption spectra were obtained with Cary 100 (Agilent, Singapore) and $BaSO_4$ as a reference. The XRD measurements were recorded on SmartLab diffractometer (Rigaku, Japan). The photoluminescence spectra were performed (Fluoromax-4, Horiba Jobin Yvon, Japan). Elemental analysis was performed on a Vario EL elemental analyzer (Germany). The zeta potential analyzer was obtained (Brookhaven Instruments Corporation, USA). XPS analysis was obtained by using a Thermo ESCALAB 250Xi instrument with a monochromatized $Al_{K\alpha}$ X-ray source (hv = 1486.6 eV). MS was operated in electrospray ionization (ESI) positive mode of accurate liquid chromatography/MS Q-TOF (LCMS-9030, Shimadzu, Japan). HPLC-MS was performed in ESI positive mode (U3000/LCQ Fleet, Thermo Scientific, USA). Flow rate was set at 0.6 mL/min: 10% of phase A (H_2O) and 90% phase B (MeOH), with column oven maintained at 35 °C. ^{13}C NMR spectra were carried on a JNM-ECZ600R spectrometer (JEOL, Japan) and all spectra were referenced to adamantane.

Computational details. The ground state geometries of all CN molecules and O_2@CN systems were optimized by DFT at the M06-2X/6-31G(d,p) level. The vibrational frequencies were calculated at the same level to confirm the optimized configurations were the minimum energy points. Based on the optimized geometries, the absorption spectra were simulated by TDDFT with M06-2X functional and 6-31G(d,p) basic set. All the above calculations were implemented in the Gaussian 16 program[53]. Besides, to obtain an insight into the characters in the excited state of electrons, the electron–hole distribution of the lowest singlet electronic excited state (S_1) in all configurations was analyzed in detail by using Multiwfn program[54].

Data availability

The data supporting the findings of this study are available within the article and its Supplementary Information, as well as from the corresponding author on reasonable request.

Received: 15 June 2020; Accepted: 3 December 2020;
Published online: 12 January 2021

References

1. Wang, S. et al. Intermolecular cascaded pi-conjugation channels for electron delivery powering CO_2 photoreduction. *Nat. Commun.* **11**, 1149 (2020).
2. Wang, X. et al. A metal-free polymeric photocatalyst for hydrogen production from water under visible light. *Nat. Mater.* **8**, 76–80 (2009).
3. Lakhi, K. et al. Mesoporous carbon nitrides: synthesis, functionalization, and applications. *Chem. Soc. Rev.* **46**, 72–101 (2017).
4. Yan, S., Li, Z. & Zou, Z. Photodegradation performance of g-C_3N_4 fabricated by directly heating melamine. *Langmuir* **25**, 10397–10401 (2009).
5. Mamba, G. & Mishra, A. Graphitic carbon nitride (g-C_3N_4) nanocomposites: a new and exciting generation of visible light driven photocatalysts for environmental pollution remediation. *Appl. Catal. B Environ.* **198**, 347–377 (2016).
6. Mane, G. et al. Highly ordered nitrogen-rich mesoporous carbon nitrides and their superior performance for sensing and photocatalytic hydrogen generation. *Angew. Chem. Int. Ed.* **56**, 8481–8485 (2017).
7. Zhou, Z., Zhang, Y., Shen, Y., Liu, S. Q. & Zhang, Y. Molecular engineering of polymeric carbon nitride: advancing applications from photocatalysis to biosensing and more. *Chem. Soc. Rev.* **47**, 2298–2321 (2018).
8. Volokh, M., Peng, G. M., Barrio, J. & Shalom, M. Carbon nitride materials for water splitting photoelectrochemical cells. *Angew. Chem. Int. Ed.* **58**, 6138–6151 (2019).
9. Huang, C. et al. Dissolution and homogeneous photocatalysis of polymeric carbon nitride. *Chem. Sci.* **9**, 7912–7915 (2018).
10. Ghosh, I. et al. Organic semiconductor photocatalyst can bifunctionalize arenes and heteroarenes. *Science* **365**, 360–366 (2019).
11. Thomas, A. et al. Graphitic carbon nitride materials: variation of structure and morphology and their use as metal-free catalysts. *J. Mater. Chem.* **18**, 4893–4908 (2008).
12. Zhang, G. et al. Optimizing optical absorption, exciton dissociation and charge transfer of a polymeric carbon nitride with ultrahigh solar hydrogen production activity. *Angew. Chem. Int. Ed.* **129**, 13630–13634 (2017).
13. Zhang, Y., Thomas, A., Antonietti, M. & Wang, X. Activation of carbon nitride solids by protonation: morphology changes, enhanced ionic conductivity, and photoconduction experiments. *J. Am. Chem. Soc.* **131**, 50–51 (2009).
14. Liu, G. et al. Unique electronic structure induced high photoreactivity of sulfur-doped graphitic C_3N_4. *J. Am. Chem. Soc.* **132**, 11642–11648 (2010).
15. Han, Q., Wang, B., Zhao, Y., Hu, C. G. & Qu, L. T. A graphitic C_3N_4 seaweed architecture for enhanced hydrogen evolution. *Angew. Chem. Int. Ed.* **54**, 11433–11437 (2016).
16. Cui, Q. et al. Phenyl modified carbon nitride quantum dots with distinct photoluminescence behavior. *Angew. Chem. Int. Ed.* **55**, 3672–3676 (2016).
17. Zhang, G., Lan, Z. & Wang, X. Surface engineering of graphitic carbon nitride polymers with co-catalysts for photocatalytic overall water splitting. *Chem. Sci.* **8**, 5261–5274 (2017).
18. Li, J. et al. Achieving efficient incorporation of pi electrons into graphitic carbon nitride for markedly improved hydrogen generation. *Angew. Chem. Int. Ed.* **58**, 1–6 (2019).
19. Yu, H. et al. Alkali-assisted synthesis of nitrogen deficient graphitic carbon nitride with tunable band structures for efficient visible-light-driven hydrogen evolution. *Adv. Mater.* **29**, 1605148 (2017).
20. Fu, J., Yu, J., Jiang, C. & Cheng, B. g-C_3N_4-based heterostructured photocatalysts. *Adv. Energy Mater.* **8**, 1701503 (2018).
21. Wang, Y. et al. Increasing solar absorption of atomically thin 2D carbon nitride sheets for enhanced visible-light photocatalysis. *Adv. Mater.* **31**, 1807540 (2019).
22. Lau, V. et al. Low-molecular-weight carbon nitrides for solar hydrogen evolution. *J. Am. Chem. Soc.* **137**, 1064–1072 (2015).
23. Lau, V. et al. Rational design of carbon nitride photocatalysts by identification of cyanamide defects as catalytically relevant sites. *Nat. Commun.* **7**, 12165 (2016).
24. Yuan, Y. et al. Microwave-assisted heating synthesis: a general and rapid strategy for large-scale production of highly crystalline g-C_3N_4 with enhanced photocatalytic H_2 production. *Green. Chem.* **16**, 4663–4668 (2014).
25. Liang, Q., Li, Z., Huang, Z. -H., Kang, F. & Yang, Q.-H. Holey graphitic carbon nitride nanosheets with carbon vacancies for highly improved photocatalytic hydrogen production. *Adv. Funct. Mater.* **25**, 6885–6892 (2015).
26. Guo, Y. et al. A Rapid Microwave-assisted thermolysis route to highly crystalline carbon nitrides for efficient hydrogen generation. *Angew. Chem. Int. Ed.* **55**, 14693–14697 (2016).
27. Lau, V. W. -H. et al. Urea-modified carbon nitrides: enhancing photocatalytic hydrogen evolution by rational defect engineering. *Adv. Energy Mater.* **7**, 1602251 (2017).
28. Zhen, W. et al. Efficient visible-light-driven selective oxygen reduction to hydrogen peroxide by oxygen-enriched graphitic carbon nitride polymers. *Energy Environ. Sci.* **11**, 2581–2589 (2018).
29. Yuan, J. et al. Positioning cyanamide defects in g-C_3N_4: engineering energy levels and active sites for superior photocatalytic hydrogen evolution. *Appl. Catal. B Environ.* **237**, 24–31 (2018).

30. Zhao, D. et al. Synergy of dopants and defects in graphitic carbon nitride with exceptionally modulated band structures for efficient photocatalytic oxygen evolution. *Adv. Mater.* **31**, 1903545 (2019).
31. Wang, W. et al. Potassium-ion-assisted regeneration of active cyano groups in carbon nitride nanoribbons: visible-light-driven photocatalytic nitrogen reduction. *Angew. Chem. Int. Ed.* **58**, 16644–16650 (2019).
32. Lin, L., Yu, Z. & Wang, X. Crystalline carbon nitride semiconductors for photocatalytic water splitting. *Angew. Chem. Int. Ed.* **58**, 6164–6175 (2019).
33. Yang, P., Zhuzhang, H., Wang, R., Lin, W. & Wang, X. Carbon vacancies in a melon polymeric matrix promote photocatalytic carbon dioxide conversion. *Angew. Chem. Int. Ed.* **58**, 1134–1137 (2019).
34. Ruan, Q., Miao, T., Wang, H. & Tang, J. Insight on shallow trap states-introduced photocathodic performance in n-type polymer photocatalysts. *J. Am. Chem. Soc.* **142**, 2795–2802 (2020).
35. Kappe, C. O. Controlled microwave heating in modern organic synthesis. *Angew. Chem. Int. Ed.* **43**, 6250–6284 (2004).
36. Zhu, Y. & Chen, F. Microwave-assisted preparation of inorganic nanostructures in liquid phase. *Chem. Rev.* **114**, 6462–6555 (2014).
37. Zhou, Z. et al. Dissolution and liquid crystals phase of 2D polymeric carbon nitride. *J. Am. Chem. Soc.* **137**, 2179–2182 (2015).
38. Lotsch, B. & Schnick, W. New light on an old story: formation of melam during thermal condensation of melamine. *Chem. Eur. J.* **13**, 4956–4968 (2007).
39. Zimmerman, J., Williams, R., Khabashesku, V. & Margrave, J. Synthesis of spherical carbon nitride nanostructures. *Nano Lett.* **1**, 731–734 (2001).
40. Ou, H., Yang, P., Lin, L., Anpo, M. & Wang, X. Carbon nitride aerogels for the photoredox conversion of water. *Angew. Chem. Int. Ed.* **56**, 10905–10910 (2017).
41. Schlomberg, H. et al. Structural insights into poly(heptazine imides): a light-storing carbon nitride material for dark photocatalysis. *Chem. Mater.* **31**, 7478–7486 (2019).
42. Zheng, Y., Lin, L., Wang, B. & Wang, X. Graphitic carbon nitride polymers toward sustainable photoredox catalysis. *Angew. Chem. Int. Ed.* **54**, 12868–12884 (2015).
43. Swift, E. A durable semiconductor photocatalyst. *Science* **365**, 320–321 (2019).
44. US EPA. *Contaminants of emerging concern including pharmaceuticals and personal care products* (U.S. Environmental protection agency Washington, DC) https://www.epa.gov/wqc/contaminants-emerging-concern-including-pharmaceuticals-and-personal-care-products (2020).
45. Dong, F. et al. In situ construction of g-C_3N_4/g-C_3N_4 metal-free heterojunction for enhanced visible-light photocatalysis. *ACS Appl. Mater. Interfaces* **5**, 11392–11401 (2013).
46. Zhang, J., Zhang, M., Sun, R. Q. & Wang, X. A facile band alignment of polymeric carbon nitride semiconductors to construct isotype heterojunctions. *Angew. Chem. Int. Ed.* **51**, 10145–10149 (2012).
47. Wang, J., Chen, Y., Shen, Y., Liu, A. & Zhang, Y. Coupling polymorphic nanostructured carbon nitrides into an isotype heterojunction with boosted photocatalytic H_2 evolution. *Chem. Commun.* **53**, 2978–2981 (2017).
48. Xiao, T. et al. In situ contruction of hierarchical WO3/g-C3N4 composite hollow microspheres as a Z-scheme photocatalyst for the degradation of antibiotics. *Appl. Catal. B Environ.* **220**, 417–428 (2018).
49. Zhang, P., Li, H. & Wang, Y. Post-functionalization of graphitic carbon nitrides by grafting organic molecules: toward C-H bond oxidation using atmospheric oxygen. *Chem. Commun.* **50**, 6312–6315 (2014).
50. Savateev, A., Ghosh, I., Koenig, B. & Antonietti, M. Photoredox catalytic organic transformations using heterogeneous carbon nitrides. *Angew. Chem. Int. Ed.* **57**, 15936–15947 (2018).
51. Zhao, T. et al. Ultrafast condensation of carbon nitride onelectrodes with exceptional boosted both photocurrent and electrochemiluminescence. *Angew. Chem. Int. Ed.* **59**, 1139–1143 (2020).
52. Peng, G., Albero, J., Garcia, H. & Shalom, M. Water-splitting carbon nitride photoelectrochemical cell with efficient charge separation and remarkably low onset potential. *Angew. Chem. Int. Ed.* **57**, 15807–15811 (2018).
53. Frisch, M. J. et al. Gaussian 16, Revision A.03 (Gaussian, Inc., Wallingford, CT, 2016).
54. Lu, T. Multiwfn Manual, version 3.6 (dev), Section 3.21.1 http://sobereva.com/multiwfn (2018).

Acknowledgements

This work was supported by the National Natural Science Foundation of China (21775018, 21675022, and 21722302), the Fundamental Research Funds for the Central Universities, the Open Funds of the State Key Laboratory of Electroanalytical Chemistry (SKLEAC201909), the Opening Project of Key Laboratory for Green Processing of Chemical Engineering of Xinjiang Bingtuan (KF2019010), and the Double-First Class project of Shihezi University (SHYL-BQ201901). We thank for Shimadzu instrumental analysis by using Q-TOF.

Author contributions

Y.Z. and C.H. conceived and designed the experiments. Y.W. and H.M. conducted first-principles density functional theory (DFT) calculations. C.H. and J.M. performed the synthesis, characterization, and activity evaluation of the catalysts. All authors contributed to the analysis and discussion of the results. C.H., Y. W., D.D., Y.S., S.L., H.M., and Y.Z. co-wrote the paper. All authors reviewed the paper.

Competing interests

The authors declare no competing interests.

Additional information

Supplementary information is available for this paper at https://doi.org/10.1038/s41467-020-20521-5.

Correspondence and requests for materials should be addressed to H.M. or Y.Z.

Peer review information *Nature Communications* thanks Gcina Mamba and the other, anonymous, reviewer(s) for their contribution to the peer review of this work. Peer reviewer reports are available.

Reprints and permission information is available at http://www.nature.com/reprints

Publisher's note Springer Nature remains neutral with regard to jurisdictional claims in published maps and institutional affiliations.